



A simulation study of a windowless gas-stripping room in an E//B neutral particle analyzer

Yuan Luo¹ · Wei-Ping Lin¹ · Pei-Pei Ren¹ · Guo-Feng Qu¹ · Jing-Jun Zhu¹ · Xing-Quan Liu¹ · Xiao-Bing Luo¹ · Zhu An¹ · Roy Wada^{2,3} · Lin-Ge Zang⁴ · Yu-Fan Qu⁴ · Zhong-Bing Shi⁴

Received: 25 April 2021 / Revised: 30 May 2021 / Accepted: 1 June 2021 / Published online: 7 July 2021
© China Science Publishing & Media Ltd. (Science Press), Shanghai Institute of Applied Physics, the Chinese Academy of Sciences, Chinese Nuclear Society 2021

Abstract The neutral particle analyzer (NPA) is one of the crucial diagnostic devices in a Tokamak facility. The stripping unit is one of the main parts of the NPA. A windowless gas-stripping room with two differential pipes has been constructed in a parallel electric and magnetic fields (E//B) NPA. The pressure distributions in the stripping chamber are simulated by ANSYS Fluent together with MolFlow+. Based on the pressure distributions obtained from the simulation, the stripping efficiency of the E//B NPA is studied using GEANT4. Hadron reaction physics is modified to track the charge state of each particle in a cross-section-based method in GEANT4. The transmission rates (R) and stripping efficiencies f_{+1} are examined for particle energies ranging from 20 to 200 keV with the input pressure (P_0), ranging from 20 to 400 Pa. According to the combined global

efficiency, $R \times f_{+1}$, $P_0 = 240$ Pa is obtained as the optimum pressure for the maximum global efficiency in the incident energy range investigated.

Keywords Neutral particle analyzer · Windowless gas-stripping chamber · Stripping efficiency · Ansys Fluent · MolFlow+ · GEANT4

1 Introduction

Tokamak is a toroidal device used in nuclear fusion research for magnetic confinement plasmas. It provides a place to test integrated technologies, materials, and physics regimes necessary for future commercial production of fusion-based electricity [1]. The neutral particle analyzer (NPA) is a crucial diagnostic device in the Tokamak facilities. It is used to determine the bulk ion temperature, isotopic ratio, and fast ion distribution of the plasma by measuring the charge exchange neutral particles escaping from the plasma. Different types of NPAs have been built in Tokamak facilities worldwide [2–13], such as the parallel direction of electric and magnetic fields (E//B) NPA on the Tokamak Fusion Test Reactor (TFTR) [2], compact neutral particle analyzer (CNPA) on the Wendelstein 7-AS stellarator [3], low- and high-energy NPAs (LENPA and HENPA) on the International Thermonuclear Experimental Reactor (ITER) [10], solid-state NPA (ssNPA) on the Experimental Advanced Superconducting Tokamak (EAST) [11], and the CP-NPA on the HuanLiuqi-2A (HL-2A) [12].

The stripping unit of the NPA plays an important role in the analysis of neutral particles, except in flux measurement NPAs, such as ssNPA [11]. It provides a place to re-ionize the charge-exchange neutral particles. According to

This work was supported by the National MCF Energy R&D Program of China (No. MOST 2018YFE0310200), the National Natural Science Foundation of China (Nos. 11805138 and 11705242), and the Fundamental Research Funds For the Central Universities (Nos. YJ201820 and YJ201954)

✉ Wei-Ping Lin
linwp1204@scu.edu.cn
Jing-Jun Zhu
zhujingjun@scu.edu.cn

- ¹ Key Laboratory of Radiation Physics and Technology of the Ministry of Education, Institute of Nuclear Science and Technology, Sichuan University, Chengdu 610064, China
- ² Cyclotron Institute, Texas A&M University, College Station, TX 77843, USA
- ³ School of Physics, Henan Normal University, Xinxiang 453007, China
- ⁴ Southwestern Institute of Physics, Chengdu 610064, China

the state of the stripping material, the stripping unit can be divided into two types: stripping foil and gas chamber. When a stripping foil is used in the NPA for low-energy neutrals, an additional accelerating or focusing voltage is required for the secondary ions [3, 9, 10]. A carbon foil with a thickness of 100 Å is commonly used as the stripping foil. In contrast, a gas chamber requires a differential pumping system when stripping gas is used. Typically, an integrated target thickness of the order of 10^{16} atoms/cm² for H₂ gas is used in the Joint European Torus (JET) NPA [13], and 10^{15} atoms/cm² for He gas is used in the E//B NPA on TFTR [2].

The energetic particles, also known as fast, superthermal, hot, and high-energy particles, are expected to play a critical role in plasma heating, current drive, momentum transport, energy transfer, and plasma stability [14, 15]. Many experimental and theoretical studies have been conducted in this field [16–20], and other related fields [21–26]. To study the frontier physics of energetic particles and to measure the fuel ratio, a new E//B NPA was designed in the present experimental devices [27]. This E//B NPA is a tandem-type NPA—similar to the CNPA built at the Ioffe Physicotechnical Institute, Russia [3]. It provides mass resolution (H and D resolution) for particles in the energy range of 20–200 keV. The magnetic field is generated with a permanent magnet for a smaller size of the NPA and easy maintenance. The upper limit energy of the E//B NPA was determined from the negative ion source neutral beam heating on the Huanliuqi-2M (HL-2M) device. The lower limit was set to 20 keV because our study focused on the fast ions instead of the background ions. For more details, refer to our previous work in Ref. [27].

In this study, a gas-stripping chamber of a new E//B NPA was designed and studied. A windowless gas-stripping chamber was adopted to avoid the replacement of the stripping foils and ensure their easy maintenance during actual operation. The performance of the gas-stripping chamber was investigated using ANSYS Fluent [28, 29] and MolFlow+ [30], together with GEANT4 [31, 32]. This article is organized as follows: The design and pressure calculation of the gas-stripping chamber is presented in Sect. 2. The results of the GEANT4 simulation and discussions are presented in Sect. 3. A brief summary is provided in Sect. 4.

2 Design and pressure calculation of the gas-stripping chamber

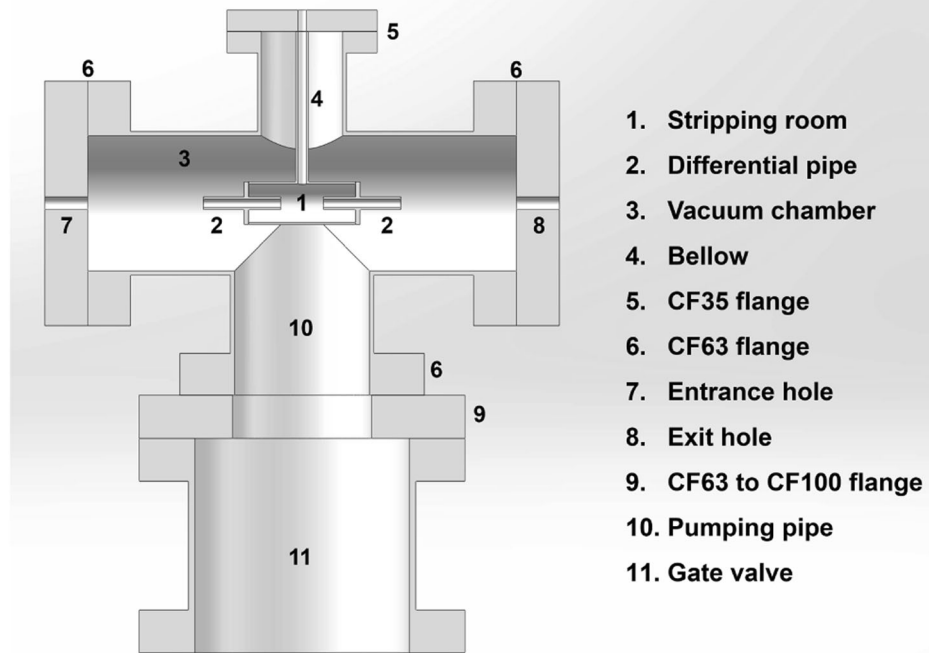
The stripping unit is one of the main parts of the NPA. The electrons of the escaped neutral particles are stripped in the stripping unit. A windowless gas-stripping chamber was adopted in the design to avoid replacement of the stripping

foil and for easy maintenance. To obtain a specific high pressure inside the stripping room and high vacuum in the outside vacuum chamber at the same time, two differential pipes with small flow conductance were used for the stripping room. Figure 1 shows the schematic layout of the stripping chamber. The stripping room (1) with two differential pipes (2) 36 mm in length and 4 mm in diameter was placed inside a vacuum chamber (3). Two holes with diameters of 6 mm (7 and 8) were made on the entrance and exit flanges to limit the beam size and maximize the vacuum isolation from the upstream pipe and downstream chamber. H₂ gas was used as the stripping gas to avoid polluting the Tokamak fuel. It was filled in the stripping room from the top flange (5) of the vacuum chamber through a bellow (4). A machinery-bearing molecular pump with a pumping speed of 340 L/s was used at the bottom of the vacuum chamber together with a gate valve (11).

The pressure distribution inside the stripping chamber is one of the main concerns in our design. A pressure of dozens of Pa is required in the stripping room to obtain sufficient stripping efficiency for high-energy hydrogen (H) and deuteron (D) atoms. In this pressure region, the gas flow state in the stripping room remains in a viscous-molecular flow state [33]. The pressure in the gas inlet and bellow was higher than that in the stripping room. On the contrary, a pressure, two or three orders of magnitude lower, was estimated in the vacuum chamber. The mean free path of the gas molecule inside the vacuum chamber is larger than the size of the chamber, and the motion of the gas molecule can be treated as collision-less. The Monte Carlo code of MolFlow+ is often used to calculate the pressure distribution of collision-less gas in a high-vacuum system. However, it is not accurate for all gas regions in the gas-stripping chamber. The computational fluid dynamics (CFD) software, which can evaluate the nonlinear effect of viscous fluid, has a better performance in the high-pressure region. However, the calculations of the CFD software in the high-vacuum region show an unnatural bump at the corners. Therefore, the gas pressure distribution of the stripping chamber was calculated by combining the CFD software of ANSYS Fluent [28, 29] (for the viscous region in the bellow, stripping room, and differential pipes) and the Monte Carlo software of MolFlow+ [30] (for the low-pressure collision-less region in the vacuum chamber).

Three-dimensional CFD calculations were performed using the ANSYS Fluent software. The fluid region was established according to the structure of the stripping chamber, as shown in Fig. 1. A laminar viscous model was adopted in the calculations. A pressure-type gas inlet was present at the top flange (5) of the vacuum chamber, and the pressure at the gas inlet P_0 ranged from 20 to 400 Pa with a step of 20 Pa set in the simulation. Three pressure-type gas outlets were present at the entrance and exit holes

Fig. 1 (Color online)
Schematic of the gas-stripping chamber



(7 and 8), and at the bottom of the gate valve (11). A pressure of 10^{-3} Pa was assumed for all three outlets. Owing to the large flow conductance of the two differential pipes (2), a small change in the outlet pressure does not affect the pressure distribution in the stripping room. Moreover, the pressure distribution in the vacuum chamber was changed based on the results from MolFlow+. Therefore, a pressure of 10^{-3} Pa at the outlets was used for all the ANSYS Fluent calculations. Stainless steel was used as the wall material. A room temperature of 300 K was used for the calculations. A typical gas flow rate of 9.97 Pa L/s was obtained at the bottom of the bellow for the input pressure $P_0 = 100$ Pa.

In the low-pressure region in the vacuum chamber (3) in Fig. 1 and inside the differential pipe (2) at $|z| > 42$ mm, where $z = 0$ was set at the center of the stripping room, the pressure distribution was simulated by MolFlow+ at the same temperature of 300 K. For the MolFlow+ simulation, the outgassing rate was adopted from the ANSYS Fluent calculations at $z = \pm 42$ mm inside the differential pipe, 4 mm from the pipe exit. For pumping, it was assumed that the gas molecules are absorbed when they hit the surfaces of the entrance and exit holes (7 and 8); that is, the sticking factor was set to 1 on the surfaces. This resulted in a pumping speed of 12.4 L/s through the entrance and exit holes. A pumping speed of 340 L/s was set at the bottom of the gate valve (11).

The simulated two-dimensional (2D) pressure distribution at $P_0 = 100$ Pa in the $y-z$ plane at $x = 0$ is shown in

Fig. 2a. The detailed pressure distribution around the stripping room is shown in Fig. 2b at a magnified scale. The pressure distribution along the beam line is shown in Fig. 2c plotted on a logarithmic scale. Using the two differential pipes in the design, the desired high pressure was achieved inside the stripping room, and a linear decrease in pressure was observed inside the two differential pipes and the entrance and exit holes. A sharp change in pressure at the entrance of the two differential pipes was observed in the ANSYS Fluent calculations. However, it was not found when MolFlow+ was used to simulate the entire gas region in the stripping chamber.

To evaluate the pressure distribution change as the pressure at the gas inlet changes, the pressures at four typical positions were examined for all the P_0 values investigated. Figure 3 shows the pressure inside the stripping room (P_1), at the entrance of the differential pipes (P_2), at the vacuum chamber (P_3), and at the outside surfaces of the entrance and exit holes (P_4), as shown in Fig. 2c as a function of pressure at the gas inlet P_0 . Linear changes in P_1 , P_2 , P_3 , and P_4 on P_0 were obtained, although slight fluctuations were observed. By using the two differential pipes in the design, the pressure in the vacuum chamber was observed to be more than 500 times lower than that in the stripping room. Through the entrance and exit holes, pressure, approximately one order of magnitude lower, was obtained for the upstream pipe and downstream chamber.

The integrated target thickness (n_T) is an important quantity in gas-stripping chambers. It is commonly used to

Fig. 2 (Color online) **a** 2D pressure distribution in the $y-z$ plane at $x=0$ for the combined simulation of ANSYS Fluent and MolFlow+ at $P_0 = 100$ Pa. **b** Magnified pressure distribution around the stripping room. **c** Pressure distribution along the beam line as a function of z on a logarithmic scale. P_1 , P_2 , P_3 , and P_4 indicate the four typical pressures in the stripping chamber

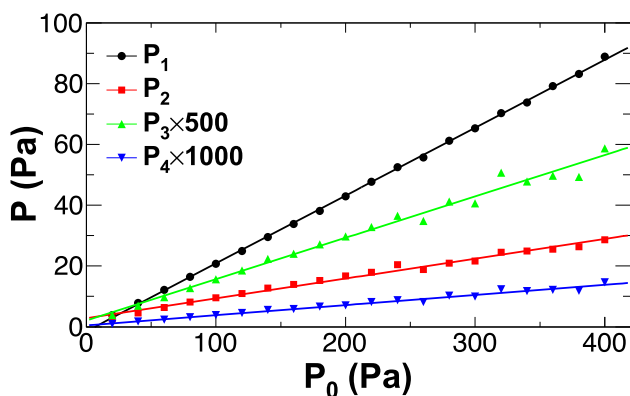
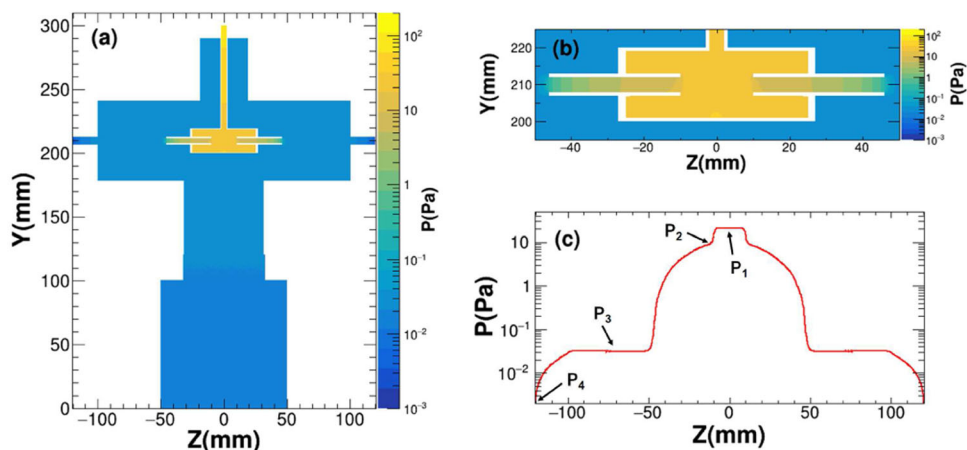


Fig. 3 (Color online) Pressure P_1 (solid circles), P_2 (solid squares), P_3 (solid triangles), and P_4 (solid inverted triangles) as a function of P_0 . The lines were obtained using linear fits

evaluate the efficiency of the stripping chamber. Because the pressures at the four typical positions were used to construct the pressure distribution in GEANT4 in the next section, a comparison of the exact n_T and the n_T calculated from the pressure distribution used in GEANT4 is necessary. Figure 4 shows n_T as a function of P_0 for the results of ANSYS Fluent and MolFlow+ (solid circles) and that of GEANT4 (open circles). A good agreement was found between them.

3 Results of GEANT4 simulation and discussion

Utilizing the obtained P_1 , P_2 , P_3 , and P_4 , the stripping efficiencies of the stripping room were further studied using GEANT4 [31, 32]. GEANT4 is a toolkit for simulating the passage of particles through matter. It has been applied in various studies, such as our previous studies on the average neutron detection efficiency for the DETecteur MODulaire de Neutrons detectors (DEMON) [34] and the module test of the Collision Centrality Detector Array (CCDA) [35], as well as many other studies of electron

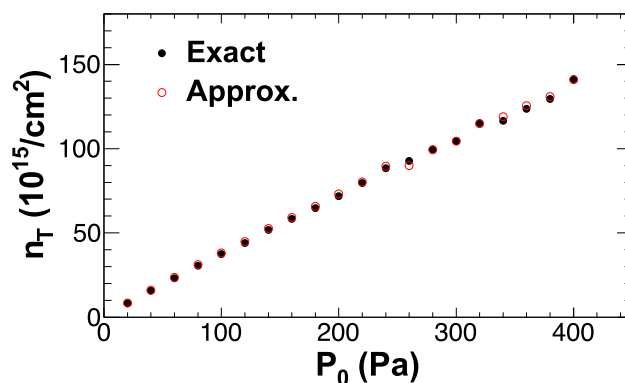


Fig. 4 (Color online) n_T as a function of P_0 . Solid circles are the exact n_T values calculated from the pressure distributions obtained from the ANSYS Fluent and MolFlow+ simulations. Open circles are the n_T values calculated from the pressure distributions constructed in the GEANT4 simulation

backscattering [36], neutron time-of-flight spectrometer system at HL-2M [37], and performance of a large-size CsI detector [38].

In the GEANT4 simulation, the physics list includes electromagnetic physics [39] and hadronic physics [40], in which ion transportation and electromagnetic, nuclear elastic, and inelastic processes are activated—although some of the processes may not be used in the actual simulation. This is because the integrated target thickness is approximately 10^{16} atoms/cm², and the scattering probability of the incident particles and the target atoms is small enough such that multi-scattering is negligible. Therefore, the G4ScreenedNuclearRecoil class [41, 42] is included in the standard electromagnetic physics for incident energies ranging from 10 eV to 100 MeV.

The charge states of the H and D atoms are the key variables in this study. However, the original GEANT4 could not properly handle the charge state. To simulate the charge state variation, the hadron reaction physics was modified to trace the charge state of each particle in a cross-section-based

method. By introducing a global charge state variable in the hadron reaction physics, the charge states of H and D were recorded when the charge exchange reaction occurred in the gas-stripping chamber. During the last century, many charge-exchange cross-section measurements have been performed for H on H₂ gas [43–54]. Figure 5 shows the electron loss cross-sections of H⁰ ($\sigma_{0,1}$), electron capture cross-sections of H⁺ ($\sigma_{1,0}$), electron capture cross-sections of H⁰ ($\sigma_{0,-1}$), and electron loss cross-sections of H⁻ ($\sigma_{-1,0}$) on H₂ gas as a function of the incident energy (E) in (a), (b), (c), and (d), respectively. Solid circles, solid squares, solid up triangles, solid down triangles, open circles, open squares, and open triangles represent the data from Gealy [45, 46], Stier [51], Barnett [43], Sanders [48], Smith [50], McClure [47], and Van Zyl [52], respectively. Solid curves represent the ORNL-recommended cross-section [53, 54]. Because the experimental $\sigma_{-1,0}$ does not cover the high-energy region at E greater than 30 keV, the ORNL recommended cross-section of the H atom on H₂ gas is used in the simulation. For a given velocity, the charge exchange cross-sections of D on Cs [55] or Rb [56] vapor are the same as those of H. Incident energies per nucleon (E/A) of H and D are the same for the investigated energy range when they have the same velocity. Therefore, the charge exchange cross-sections of H are also used for D at the same E/A in the simulations.

The simulations were performed for H and D on H₂ gas with incident energies ranging from 20 to 200 keV in steps of 20 keV and with P_0 ranging from 20 to 400 Pa in steps of 20 Pa. H and D atoms are generated at the entrance hole

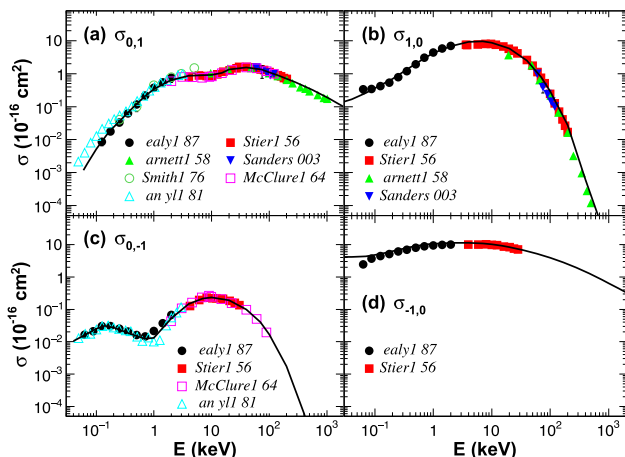


Fig. 5 (Color online) Charge exchange cross-section of $\sigma_{0,1}$ (a), $\sigma_{1,0}$ (b), $\sigma_{0,-1}$ (c), and $\sigma_{-1,0}$ (d) in the order of of 10^{-16} cm² per molecule as a function of the incident energy (E) of the H atom or ion. Solid circles, solid squares, solid up triangles, solid down triangles, open circles, open squares, and open triangles represent the data from Gealy [45, 46], Stier [51], Barnett [43], Sanders [48], Smith [50], McClure [47], and Van Zyl [52], respectively. The solid curves represent the ORNL-recommended cross-section [53, 54], which is also used in the simulation

(7) of the vacuum chamber, corresponding to the z position of -120 mm, and distributed uniformly on the entrance hole surface with the same diameter of 6 mm. The momentum direction was assumed to be parallel to the z -axis. One million events were generated for each run. The energy losses ($\Delta E/E$) of H and D at 20 keV as a function of P_0 are shown in Fig. 6. A slightly lower energy loss is observed for D because the mass of D is twice that of H, which causes less energy loss during the collisions. It can be seen from Fig. 6 that H and D increase linearly as P_0 increases. The maximum energy loss of 20 keV for H and D was less than 4% for all P_0 investigated. Compared to the energy resolution of this NPA, the energy losses of H and D after passing through the stripping chamber are small and can be neglected.

Because the diameters of the two differential pipes are smaller than these of the entrance and exit holes, some of the incident particles will be stopped by the geometry of the stripping chamber. Moreover, owing to the Coulomb scattering of the incident particles and the target atoms, some of the incident particles are scattered away from their original directions. Therefore, the transmission rate (R) of the incident particles is important, especially for low-energy particles that suffer more Coulomb scattering when they pass through the stripping chamber. In this study, the transmission rate is defined as the ratio between the number of particles reached at the exit hole (8) after passing through the stripping chamber with H₂ gas ($P_0 > 0$ Pa) and that without the gas ($P_0 = 0$ Pa, vacuum). Thus, the particle loss caused by the geometry of the stripping chamber was canceled out. Figure 7 shows the transmission rate as a function of the incident energy for $P_0 = 20$ Pa (circles), 100 Pa (squares), and 400 Pa (triangles) in (a); and as a function of P_0 for the incident energy $E = 20$ keV (circles), 40 keV (squares), and 100 keV (triangles) in (b). The solid and open symbols represent H and D,

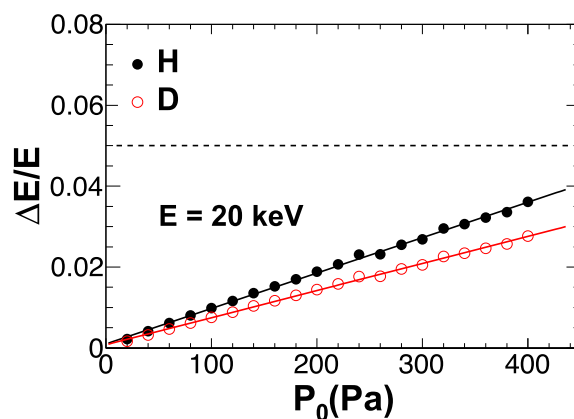


Fig. 6 (Color online) Energy loss of 20 keV for H and D passing through the stripping chamber as a function of P_0 . The dashed line shows the guideline for $\Delta E/E = 0.05$. Solid lines represent linear fits

respectively. A slight increasing trend was observed for the transmission rate as the incident energy increased, but it showed an opposite trend as P_0 increased. The scattering loss was small (less than 3%) for all the investigated incident energies and input pressures.

The stripping efficiency in the stripping chamber was evaluated using the charge fraction variable (f) for the incident particles after the stripping area. The evolution of the charge fraction inside the stripping area is the most important aspect of this study. Figure 8 shows the charge state fraction as a function of the z position in the stripping chamber for H and D atoms at 20, 100, and 200 keV. The pressures used in the simulation are those from the results of $P_0 = 100$ Pa, as shown in Sect. 2. The solid, dashed, and long-dashed curves correspond to the fractions of the charge states 0, +1, and -1, respectively. Owing to the small cross-section of $\sigma_{0,-1}$, the fraction of charge state -1 is less than 2% for H and D at an incident energy of 20 keV and becomes negligible for higher incident energies. The fraction of charge states 0 and +1 shows a sharp change starting from around $z = -40$ mm, which is because the stripping room is located at $-46 \text{ mm} < z < 46 \text{ mm}$. Owing to the energy dependence of the charge exchange cross-section, particles with lower incident energies have smaller saturation thicknesses for the charge fractions. The higher stripping efficiency for particles with larger energies is mainly caused by the sharp decrease in $\sigma_{1,0}$ as the incident energy increases.

Figure 9 shows the fraction of charge state +1 (f_{+1}) at $z = 120$ mm as a function of E/A for $P_0 = 20$ Pa (circles), 100 Pa (squares) and 400 Pa (triangles) in (a), and as a function of P_0 for the incident energy $E = 20$ keV (circles), 100 keV (squares) and 200 keV (triangles) in (b). Solid and open symbols represent H and D, respectively. One can see from Fig. 9a that f_{+1} increases at lower incident energies for different P_0 up to E/A around 100 keV. After reaching the maximum value, f_{+1} decreases for $P_0 = 20$ Pa, and stays

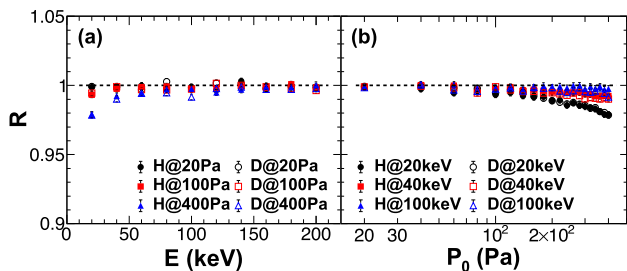


Fig. 7 (Color online) **a** R as a function of E . Circles, squares, and triangles represent $P_0 = 20, 100,$ and 400 Pa, respectively. **b** R as a function of P_0 . Circles, squares, and triangles represent those at $P_0 = 20, 40,$ and 100 keV, respectively. The solid and open symbols represent H and D, respectively. The dashed lines show that for $R = 1$. The errors shown for the data points were statistical errors

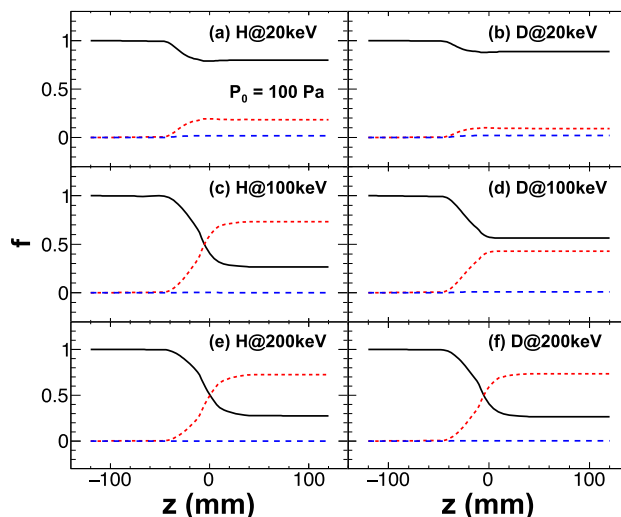


Fig. 8 (Color online) Charge state fraction as a function of z position in the stripping chamber for H at 20 keV in (a), D at 20 keV in (b), H at 100 keV in (c), D at 100 keV in (d), H at 200 keV in (e), and D at 200 keV in (f). The pressures used in the simulation were those from the results of $P_0 = 100$ Pa. The solid, dashed, and long-dashed curves correspond to the fractions of charge states 0, +1, and -1, respectively

flat for $P_0 = 100$ Pa, but keeps slowly increasing for $P_0 = 400$ Pa as E/A increases. This indicates that the thickness of the stripping gas is not enough for higher energy particles at $P_0 = 20$ Pa. No noticeable difference between H and D is observed, indicating that the results can also be applied to neutral tritium particles when E/A is used. As shown in Fig. 9b, the fractions of charge state +1 quickly reach a maximum value and keep the maximum as P_0 increases at lower E . For larger E , the fractions increase faster at lower P_0 and reach the maximum at a pressure of around $P_0 = 240$ Pa.

To verify the GEANT4 results, f_{+1} is also calculated using the gas-integrated target thickness (n_T) as

$$f_{+1} = \frac{\sigma_{01}}{\sigma_{01} + \sigma_{10}} \{1 - \exp[-n_T(\sigma_{01} + \sigma_{10})]\}, \quad (1)$$

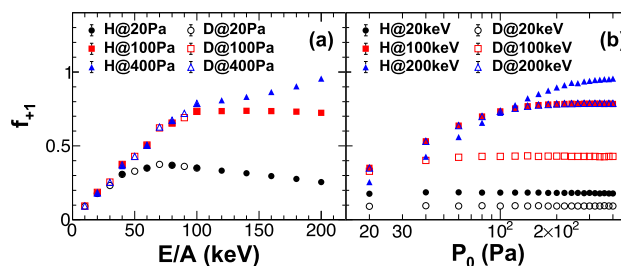


Fig. 9 (Color online) **a** f_{+1} as a function of E/A . Circles, squares, and triangles represent the values at $P_0 = 20, 100,$ and 400 Pa, respectively. **b** f_{+1} as a function of P_0 . Circles, squares, and triangles represent the values at $E = 20, 100,$ and 200 keV, respectively. The solid and open symbols represent H and D, respectively

σ_{01} and σ_{10} are the stripping (electron loss) and charge exchange (electron capture) cross-sections of H(D) and $H^+(D^+)$, respectively. The small amount of particle loss due to the electron capture of H(D), σ_{0-1} , and σ_{-10} , is neglected in Eq. (1). The results are shown in Fig. 10. The symbols are the same f_{+1} values from the GEANT4 simulation in Fig. 9b but plotted as a function of n_T , and the solid and dashed lines are those from Eq. (1) for H and D, respectively. Good agreement was found between the calculations and GEANT4 simulations. These good agreements originate from the following facts: In the GEANT4 simulation, the evaluation of f_{+1} is obtained from a Monte Carlo sampling of the charge state along the particle track according to the cross-sections of σ_{01} , σ_{10} , σ_{0-1} , and σ_{-10} . As mentioned earlier, in Eq. (1), only a part of the cross-sections (σ_{01} and σ_{10}) is used, neglecting σ_{0-1} and σ_{-10} , because the latter values are orders of magnitude smaller.

To determine the optimum condition, the global efficiency, a combination of transmission rate and fraction of charge state +1, $R \times f_{+1}$, was further studied. Figure 11 shows the global efficiency of $R \times f_{+1}$ as a function of P_0 for the incident energies $E = 20, 100,$ and 200 keV in (a), (b), and (c), and as a function of n_T in (d), (e), and (f), respectively. The global efficiency of H and D decreases gradually as the pressure P_0 increases for $E = 20$ keV. On the other hands, the global efficiency shows a trend similar to that of f_{+1} as the pressure P_0 increases for $E = 100$ and 200 keV. For pressures $P_0 > 240$ Pa, the global efficiency becomes flat for all conditions of H and D at the incident energy $E \geq 100$ keV. Considering the low temperature of the plasma in HL-2A/M, the number of high-energy particles is orders of magnitude lower than that of the low-energy particles. Therefore, $P_0 = 240$ Pa was obtained as the optimum pressure for the maximum global efficiency in the incident energy range investigated. At this P_0 , the pressure in the vacuum chamber is less than 0.1 Pa, which

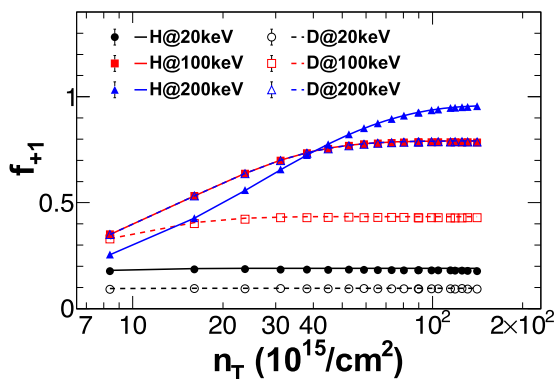


Fig. 10 (Color online) The fraction of H^+ (solid symbols) and D^+ (open symbols) as a function of n_T for $E = 20$ keV (circles), 100 keV (squares), and 200 keV (triangles). The solid and dashed lines represent the results of Eq. (1). More details are provided in the text

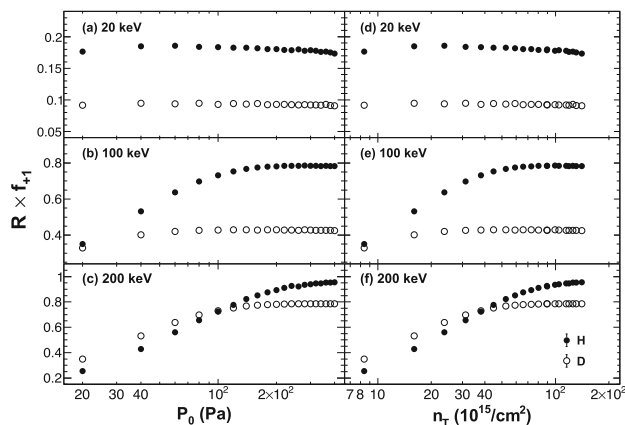


Fig. 11 Global efficiency of $R \times f_{+1}$ as a function of the pressure P_0 for incident energies $E = 20$ keV (a), 100 keV (b), and 200 keV (c–f) is the same as those in a–c—but as a function of n_T . The solid and open circles represent H and D, respectively.

is within the operating pressure range of the molecular pump. The simulation results would provide a useful guide for practical applications.

4 Summary

The neutral particle analyzer (NPA) is a crucial diagnostic device in Tokamak facilities. The stripping unit is one of the main parts of NPA. A windowless gas tripping room with two differential pipes was adopted to maintain a certain pressure in the parallel electric and magnetic fields (E//B) NPA. The gas pressure distribution of the stripping chamber was calculated by combining the computational fluid dynamics (CFD) software ANSYS Fluent, and the Monte Carlo software MolFlow+ for the low-pressure collision-less region in the vacuum chamber. The pressure distribution along the beam direction was obtained for different input pressures. A certain high pressure was achieved inside the stripping room, and a linear decreasing pressure was obtained inside the differential pipes and the entrance and exit holes. A pressure more than two orders smaller was obtained in the vacuum chamber than that inside the stripping room.

Based on the pressure distributions calculated by ANSYS Fluent and MolFlow+, the stripping efficiency of the stripping chamber for H and D atoms at incident energies ranging from 20 to 200 keV was studied using GEANT4. The energy losses of H and D after passing through the stripping chamber are small and can be neglected for all the investigated incident energies and input pressures. The scattering loss of H and D atoms on H_2 gas was studied using the transmission rate (R) of the incident atoms. A slight increasing trend was observed for R as the incident energy increased, but showed an opposite

trend as the input pressure (P_0) increased. The scattering loss is small (less than 3%) for all the investigated incident energies and input pressures.

A charge state variable was introduced to track the charge state of the particles in the GEANT4 simulation. Adopting the ORNL-recommended charge exchange cross-sections with modified hadron reaction physics, the charge state of each particle is traced in the simulation. The behaviors of the charge fractions along the beam direction (z -axis) in the H_2 gas were investigated for $E = 20, 100,$ and 200 keV H and D atoms. The stripping efficiency was obtained as the fraction of charge state $+1$ at the exit hole of the vacuum chamber ($z = 120$ mm). After reaching the maximum value, f_{+1} decreases for $P_0 = 20$ Pa, and remains flat for $P_0 = 100$ Pa, but continues to increase slowly for $P_0 = 400$ Pa as the incident energy per nucleon increases. f_{+1} quickly reaches a maximum value and maintains the maximum as P_0 increases at lower E . For larger E , the fractions increase faster at lower P_0 and reach a maximum at an input pressure of approximately $P_0 = 240$ Pa.

According to the combined global efficiency, $R \times f_{+1}$, $P_0 = 240$ Pa was found to be the optimum pressure for the maximum global efficiency in the incident energy range investigated. The simulation results would provide a useful guide for practical applications.

Author Contributions All authors contributed to the study conception and design. Material preparation, data collection, and analysis were performed by Yuan Luo and Wei-Ping Lin. The first draft of the manuscript was written by Yuan Luo and all authors commented on previous versions of the manuscript. All authors read and approved the final manuscript.

References

1. ITER. <https://www.iter.org/>
2. S.S. Medley, A.L. Roquemore, Construction and operation of parallel electric and magnetic field spectrometers for mass/energy resolved multi-ion charge exchange diagnostics on the Tokamak Fusion Test Reactor. *Rev. Sci. Instrum.* **69**, 2651 (1998). <https://doi.org/10.1063/1.1148994>
3. F.V. Chernyshev, V.I. Afanasyev, A.V. Dech et al., A compact neutral-particle analyzer for plasma diagnostics. *Instrum. Exp. Tech.* **47**, 214 (2004). <https://doi.org/10.1023/B:INET.0000025204.01783.1a>
4. S.Y. Petrov, V.I. Afanasyev, A.D. Melnik et al., Design features of the neutral particle diagnostic system for the ITER tokamak. *Phys. At. Nucl.* **80**, 1268 (2017). <https://doi.org/10.1134/S1063778817070109>
5. M. Isobe, M. Sasao, Charge exchange neutral particle analysis with natural diamond detectors on LHD heliotron. *Rev. Sci. Instrum.* **72**, 611 (2001). <https://doi.org/10.1063/1.1318250>
6. V.A. Krasilnikov, A.V. Krasil'nikov, D.A. Skopintsev et al., A diamond-detector-based system for spectrometry of fast atoms on the JET tokamak. *Instrum. Exp. Tech.* **51**, 258–262 (2008). <https://doi.org/10.1134/S0020441208020188>
7. G. Bracco, G. Betello, S. Mantovani et al., Design and calibration of the JET time of flight neutral particle analyzer with high noise rejection capability. *Rev. Sci. Instrum.* **63**, 5685 (1992). <https://doi.org/10.1063/1.1143350>
8. D. Liu, W.W. Heidbrink, K. Tritz et al., Compact and multi-view solid state neutral particle analyzer arrays on National Spherical Torus Experiment-Upgrade. *Rev. Sci. Instrum.* **87**, 11D803 (2016). <https://doi.org/10.1063/1.4959798>
9. V.I. Afanasyev, A. Gondhalekar, PYu. Babenko et al., Neutral particle analyzer/isotope separator for measurement of hydrogen isotope composition of JET plasmas. *Rev. Sci. Instrum.* **74**, 2338 (2003). <https://doi.org/10.1063/1.1542664>
10. V.I. Afanasyev, F.V. Chernyshev, A.I. Kislyakov et al., Neutral particle analysis on ITER: present status and prospects. *Nucl. Instrum. Methods A* **621**, 456 (2010). <https://doi.org/10.1016/j.nima.2010.06.201>
11. J.Z. Zhang, Y.B. Zhu, J.L. Zhao et al., First results from solid state neutral particle analyzer on experimental advanced superconducting tokamak. *Rev. Sci. Instrum.* **87**, 11D834 (2016). <https://doi.org/10.1063/1.4962063>
12. W. Li, Z.W. Xia, J. Lu et al., A new neutral particle analyzer diagnostic and its first commissioning on HL-2A. *Rev. Sci. Instrum.* **83**, 10D702 (2012). <https://doi.org/10.1063/1.4729494>
13. R. Bartiromo, G. Bracco, M. Brusati et al., Design and calibration of the JET neutral particle analyzer. *Rev. Sci. Instrum.* **58**, 788 (1987). <https://doi.org/10.1063/1.1139634>
14. W. Chen, Z.X. Wang, Energetic particles in magnetic confinement fusion plasmas. *Chin. Phys. Lett.* **37**, 125001 (2020). <https://doi.org/10.1088/0256-307X/37/12/125001>
15. L. Chen, F. Zonca, Physics of Alfvén waves and energetic particles in burning plasmas. *Rev. Mod. Phys.* **88**, 015008 (2016). <https://doi.org/10.1103/RevModPhys.88.015008>
16. P.W. Shi, W. Chen, X.R. Duan, Energetic particle physics on the HL-2A tokamak: a review. *Chin. Phys. Lett.* **38**, 035202 (2021). <https://doi.org/10.1088/0256-307X/38/3/035202>
17. Y. Chen, W.L. Zhang, J. Bao et al., Verification of energetic-particle-induced geodesic acoustic mode in gyrokinetic particle simulations. *Chin. Phys. Lett.* **37**, 095201 (2020). <https://doi.org/10.1088/0256-307X/37/9/095201>
18. B. Madsen, J. Huang, M. Salewski et al., Fast-ion velocity-space tomography using slowing-down regularization in EAST plasmas with co- and counter-current neutral beam injection. *Plasma Phys. Control. Fusion* **62**, 115019 (2020). <https://doi.org/10.1088/1361-6587/abb79b>
19. N.N. Gorelenkov, D. Pinches, K. Toi et al., Energetic particle physics in fusion research in preparation for burning plasma experiments. *Nucl. Fusion* **54**, 125001 (2014). <https://doi.org/10.1088/0029-5515/54/12/125001>
20. X.T. Ding, W. Chen, Review of the experiments for energetic particle physics on HL-2A. *Plasma Sci. Technol.* **20**, 094008 (2018). <https://doi.org/10.1088/2058-6272/aad27a>
21. S.Z. Wei, Y.H. Wang, P.W. Shi et al., Nonlinear coupling of reversed shear Alfvén eigenmode and toroidal Alfvén eigenmode during current ramp. *Chin. Phys. Lett.* **38**, 035201 (2021). <https://doi.org/10.1088/0256-307X/38/3/035201>
22. J.Q. Xu, X.D. Peng, H.P. Qu et al., Stabilization of short wavelength resistive ballooning modes by ion-to-electron temperature and gradient ratios in tokamak edge plasmas. *Chin. Phys. Lett.* **37**, 062801 (2020). <https://doi.org/10.1088/0256-307X/37/6/062801>
23. B.N. Wan and EAST team, A new path to improve high β_p plasma performance on EAST for steady-state tokamak fusion reactor. *Chin. Phys. Lett.* **37**, 045202 (2020). <https://doi.org/10.1088/0256-307x/37/4/045202>

24. B.W. Zheng, C.Y. Jiang, Z.H. Liu et al., Correction and verification of HL-2A Tokamak Bonner sphere spectrometer in monoenergetic neutron fields from 100 keV to 5 MeV. *Nucl. Sci. Tech.* **30**, 159 (2019). <https://doi.org/10.1007/s41365-019-0689-9>
25. S.B. Shu, C.M. Yu, C. Liu et al., Improved plasma position detection method in EAST Tokamak using fast CCD camera. *Nucl. Sci. Tech.* **30**, 24 (2019). <https://doi.org/10.1007/s41365-019-0549-7>
26. Z.X. Cui, X. Li, S.B. Shu et al., Calculation of the heat flux in the lower divertor target plate using an infrared camera diagnostic system on the experimental advanced superconducting tokamak. *Nucl. Sci. Tech.* **30**, 94 (2019). <https://doi.org/10.1007/s41365-019-0625-z>
27. L. Zang, Y.F. Qu, W.P. Lin et al., Design of the electromagnetic field for an E//B neutral particle analyzer. *Plasma Fusion Res.* **15**, 2402036 (2020). <https://doi.org/10.1585/pfr.15.2402036>
28. ANSYS. <https://www.ansys.com/>
29. B. Mohamedi, S. Hanini, A. Ararem et al., Simulation of nucleate boiling under ANSYS-FLUENT code by using RPI model coupling with artificial neural networks. *Nucl. Sci. Tech.* **26**, 040601 (2015). <https://doi.org/10.13538/j.1001-8042/nst.26.04060110.13538/j.1001-8042/nst.26.040601>
30. M. Ady, R. Kersevan, Introduction to the latest version of the test-particle Monte Carlo code molflow+, in *Proceeding of the 10th Int. Particle Accelerator Conf., Dresden, Germany, June 2014*, pp. 2348-2350. <https://doi.org/10.18429/JACoW-IPAC2019-TUPMP037>
31. S. Agostinelli, J. Allison, K. Amako et al., Geant4—a simulation toolkit. *Nucl. Instrum. Methods A* **506**, 250 (2003). [https://doi.org/10.1016/S0168-9002\(03\)01368-8](https://doi.org/10.1016/S0168-9002(03)01368-8)
32. J. Allison, K. Amako, J. Apostolakis et al., Recent developments in Geant4. *Nucl. Instrum. Methods A* **835**, 186 (2016). <https://doi.org/10.1016/j.nima.2016.06.125>
33. D. Da, *The Vacuum Design Manuals*, 3rd edn. (National Defence Industry Press, Beijing, 2004), p. 7
34. S. Zhang, W. Lin, M.R.D. Rodrigues et al., Average neutron detection efficiency for DEMON detectors. *Nucl. Instrum. Methods A* **709**, 68 (2013). <https://doi.org/10.1016/j.nima.2013.01.039>
35. F. Fen, W.P. Lin, X.Q. Liu et al., A module test of CCDA: an array to select the centrality of collisions in heavy ion collisions. *Chin. Phys. Lett.* **31**, 082502 (2014). <https://doi.org/10.1088/0256-307X/31/8/082502>
36. P. Dondero, A. Mantero, V. Ivanchenko et al., Electron backscattering simulation in Geant4. *Nucl. Instrum. Methods B* **425**, 18 (2018). <https://doi.org/10.1016/j.nimb.2018.03.037>
37. B. Zheng, W. Zhang, T. Wu et al., Development of the real-time double-ring fusion neutron time-of-flight spectrometer system at HL-2M. *Nucl. Sci. Tech.* **30**, 175 (2019). <https://doi.org/10.1007/s41365-019-0702-3>
38. H. Dong, D. Fang, C. Li, Study on the performance of a large-size CsI detector for high energy γ -rays. *Nucl. Sci. Tech.* **29**, 7 (2018). <https://doi.org/10.1007/s41365-017-0345-1>
39. S. Incerti, V. Ivanchenko, M. Novak et al., Recent progress of Geant4 electromagnetic physics for calorimeter simulation. *J. Inst.* **13**, C02054 (2018). <https://doi.org/10.1088/1748-0221/13/C02054>
40. J.P. Wellisch, Hadronic shower models in Geant4—the frameworks. *Comput. Phys. Commun.* **140**, 65 (2001). [https://doi.org/10.1016/S0010-4655\(01\)00256-9](https://doi.org/10.1016/S0010-4655(01)00256-9)
41. R.A. Weller, M.H. Mendenhall, D.M. Fleetwood, A screened Coulomb scattering module for displacement damage computations in Geant4. *IEEE Trans. Nucl. Sci.* **51**, 3669 (2004). <https://doi.org/10.1109/TNS.2004.839643>
42. M.H. Mendenhall, R.A. Weller, An algorithm for computing screened Coulomb scattering in Geant4. *Nucl. Instrum. Methods B* **227**, 420 (2005). <https://doi.org/10.1016/j.nimb.2004.08.014>
43. R.O. Simmons, R.W. Balluffi, X-ray study of deuterium-irradiated copper near 10° K. *Phys. Rev.* **109**, 355 (1958). <https://doi.org/10.1103/PhysRev.109.355>
44. R. Curran, T.M. Donahue, Electron capture and loss by hydrogen atoms in molecular hydrogen. *Phys. Rev.* **118**, 1233 (1960). <https://doi.org/10.1103/PhysRev.118.1233>
45. M.W. Gealy, B. Van Zyl, Cross sections for electron capture and loss. I. H^+ and H^- impact on H and H_2 . *Phys. Rev. A* **36**, 3091 (1987). <https://doi.org/10.1103/physreva.36.3091>
46. M.W. Gealy, B. Van Zyl, Cross sections for electron capture and loss. II. H impact on H and H_2 . *Phys. Rev. A* **36**, 3100 (1987). <https://doi.org/10.1103/physreva.36.3100>
47. G.W. McClure, Ionization and dissociation of fast H_2 molecules incident on H_2 gas. *Phys. Rev.* **134**, A1126 (1964). <https://doi.org/10.1103/PhysRev.134.A1226>
48. J.M. Sanders, S.L. Varghese, C.H. Fleming et al., Electron capture by protons and electron loss from hydrogen atoms in collisions with hydrocarbon and hydrogen molecules in the 60–120 keV energy range. *J. Phys. B At. Mol. Opt. Phys.* **36**, 3835 (2003). <https://doi.org/10.1088/0953-4075/36/18/311>
49. G.M. Sigaud, Free-collision model calculations for projectile electron loss by the H_2 molecule. *J. Phys. B At. Mol. Opt. Phys.* **44**, 225201 (2011). <https://doi.org/10.1088/0953-4075/44/22/225201>
50. K.A. Smith, M.D. Duncan, M.W. Geis et al., Measurement of electron loss cross sections for 0.25- to 5-keV hydrogen atoms in atmospheric gases. *J. Geophys. Res.* **81**, 2231 (1976). <https://doi.org/10.1029/JA081i013p02231>
51. P.M. Stier, C.F. Barnett, Charge exchange cross sections of hydrogen ions in gases. *Phys. Rev.* **103**, 896 (1956). <https://doi.org/10.1103/PhysRev.103.896>
52. B. Van Zyl, T.Q. Le, R.C. Amme, Charged particle production in low energy H^+ H_2 and $H+He$ collisions. *J. Chem. Phys.* **74**, 314 (1981). <https://doi.org/10.1063/1.440836>
53. H.T. Hunter, M.I. Kirkpatrick, I. Alvarez et al., Atomic data for fusion, ORNL-6086/V1. United States (1990). <https://doi.org/10.2172/6570226>
54. D.R. Schultz, H. Gharibnejad, T.E. Cravens et al., Data for secondary-electron production from ion precipitation at Jupiter III: target and projectile processes in H^+ , H, and $H^- + H_2$ collisions. *At. Data Nucl. Data* **132**, 101307 (2020). <https://doi.org/10.1016/j.adt.2019.101307>
55. F.W. Meyer, L.W. Anderson, Charge exchange cross sections for hydrogen and deuterium ions incident on a Cs vapor target. *Phys. Lett. A* **54**, 333 (1975). [https://doi.org/10.1016/0375-9601\(75\)90282-0](https://doi.org/10.1016/0375-9601(75)90282-0)
56. A.S. Schlachter, P.J. Bjorkholm, D.H. Loyd et al., Charge-exchange collisions between hydrogen ions and cesium vapor in the energy range 0.5–20 keV. *Phys. Rev.* **177**, 184 (1969). <https://doi.org/10.1103/PhysRev.177.184>